Chapter 8
The Role of the Ponderomotive Force in High Field Experiments

Luis Roso, José Antonio Pérez-Hernández, Roberto Lera, and Robert Fedosejevs

Abstract Petawatt lasers are a new tool to understand many basic properties of matter (solids, plasmas, molecules, atoms, and nuclei) in extreme conditions. Radiation reaction and fundamental non-linear QED problems can also be studied with high intensity lasers, as well as many other relevant problems. In all cases we focus the laser to concentrate its energy over a small volume, therefore a huge intensity gradient appears, and it generates a force -the ponderomotive force- that drives the ionized electrons. This driving can be dominant in some situations. A conventional focus has a convex intensity pattern and ponderomotive force expels the electrons out of the focal region. With optimal use of TEM 01 and 10 modes it is possible to generate concave beams that trap and drag such electrons. Such possibilities are reviewed here, particularly for the strongly relativistic intensities available with existing ultraintense lasers.

8.1 Introduction

Origins of the ponderomotive force

A charged particle inside an oscillating electric field experiences a quiver motion and therefore has an average energy larger than zero, even if its motion is perfectly oscillatory and the average displacement is zero. Because the charged particle has an energy larger inside the field than outside the field, there is a force that tends to move it out of the high field region. The potential responsible for this force is known as the ponderomotive potential.

L. Roso (✉) · J. A. Pérez-Hernández · R. Lera
Center for Pulsed Lasers, CLPU, 37185 Villamayor, Salamanca, Spain
e-mail: roso@clpu.es

L. Roso
Applied Physics Department, Universidad de Salamanca, 37008 Salamanca, Spain

R. Fedosejevs
Electrical and Computer Engineering, University of Alberta, Edmonton, AB T6G 2V4, Canada

K. Yamanouchi et al. (eds.), *Progress in Ultrafast Intense Laser Science XVI*,
Topics in Applied Physics 141, https://doi.org/10.1007/978-3-030-75089-3_8

This idea was first developed, well before the arrival of lasers, for radiofrequency waves. The first relativistic description was given in 1966 by Kibble [1] under a very appealing name: *mutual refraction of electrons and photons*. Ponderomotive forces were regarded as forces that modify the average trajectory of an accelerated electron crossing a laser field. As the electron enters the laser field its direction is deflected similar to refraction of light. This similarity is very physical and gives a lot of insight to the problem that has been lost in modern literature about this subject. Kibble also studied key features of the standing wave dynamics.

Today's superintense lasers

Since the invention of the CPA technology by Strickland and Mourou [2], ultraintense lasers have increased in performance dramatically. Petawatt (PW), or multi PW, lasers are a reality now [3] and soon the 10 PW barrier will be broken in several facilities around the world. Peak power gives the possibility to focus to extreme intensities, and intensity is the key to induce extreme effects. A focal spot close to diffraction limited quality requires a good optical quality laser pulse, very precise beam transport and a good focusing mirror (typically an off axis parabolic mirror). In order to suppress nonlinear effects, every element after the amplification chain, including the pulse compressor is kept under high vacuum, typically 10^{-6} mbar.

Laser acceleration

Particle accelerators are a fundamental tool in many fields of science and technology. Besides the TeV particle accelerators such as CERN LHC, designed to study the fundamental building blocks of matter, there are many other systems used to advance material science, biology, chemistry, and many more fields. Such accelerators reach up to GeV energies for electrons after many meters, if not kilometers of acceleration. We know today about the potential of ultra-intense lasers for particle acceleration, particularly for electron acceleration, offering the possibility to achieve similar energy per particle as conventional accelerators but in just a fraction of the size. Laser acceleration of electrons uses collective plasma effects to generate, over a very short period of time, enormous field gradients which have proved to be a very efficient tool to accelerate GeV electrons over a short distance (of the order of one or several centimeters) [4–6]. One of the most studied mechanisms is Laser Wakefield Acceleration (LWFA), where the acceleration of particles is generated inside the wake of a high intensity laser pulse as it travels through an underdense plasma medium. The result is a strong longitudinal electric field that couples to the electrons trapped inside this wave induced by the driving laser, accelerating those electrons over the distance of the plasma channel. Since there is no breakdown limit in plasma, the resulting accelerating gradient is huge [7]. Applications of this mechanism include the generation of ultrashort coherent x-ray beams produced by betatron radiation of the accelerated oscillating electrons, which have potential to be used in a wide range of fields [8].

However, plasma effects are quite nonlinear and subject to intrinsic instabilities and for that reason there is renewed interest in direct acceleration of electrons by a laser field as a potential candidate for laser electron acceleration. The idea of such

direct laser acceleration (we call it direct because it does not need the presence of collective plasma effects) has been attracting a lot of interest during recent decades [9]. In laser acceleration, the electron enters and leaves the beam and the goal is to find the best configuration of fields that provides acceleration.

The aim of this work is to show the effects of the ponderomotive force when a gas is ionized during the turn-on and electrons are driven by the focused beam. Released electrons will be subject to an inhomogeneous electromagnetic field and therefore the ponderomotive force will be fundamental for their dynamics. We are not going to consider situations where electrons are injected at relativistic speeds. Instead we will study something related but conceptually different. We consider electrons ionized during the turn-on of the pulse, so they are born inside the field and we want to see how they move. Our purpose is not to study their final speed after leaving the intense pulse. We are going to study their dynamics while in the field and describe common experimental situations seen from a different viewpoint. We will describe several common experimental situations where such ponderomotive force is present but maybe has not been not properly taken into account, as well as other less considered situations where the ponderomotive force presents interesting features. In most cases the electron cloud will explode, but in other cases part of the cloud can be redirected to one side or trapped inside the field.

Experimental situation

A typical high-intensity experiment is performed in high vacuum. The pulse has to be focused to a tiny spot (microns) in order to reach ultrahigh intensities and interact with a target, that can be a solid, liquid or a gas. Gas targets, which take the form of gas jets, gas cells or capillaries, are of special interest for the sake of this discussion since they are employed in underdense plasma physics experiments such as coherent x-ray sources or LWFA. Gas jets are usually delivered through a pulsed nozzle, which is close to the focal spot, and the gas is released a few milliseconds before the arrival of the pulse. As a consequence, the laser pulse hits a diluted neutral gas and atoms or molecules are ionized in the leading edge of the pulse (by barrier suppression), so electrons are released well before its peak. In this regime pondermotive force is fundamental because it causes electrons to move towards weaker field regions therefore deflecting them out of the ultrahigh intensity region. This force avoids to some extent extreme effects (extreme acceleration, extreme radiation, etc.). We will analyze, based on numerical simulations of the relativistic driven independent electron trajectories, how to control and take profit of this ponderomotive repulsion.

Since the model neglects collective effects, it will be valid just for dilute targets. For solid targets, usually few micron thick foils, liquid and overdense plasma experiments, the study of the ponderomotive force needs to include also the fields generated at the target, and this is outside the scope of the present text.

A third family of targets are the electron injectors. Electrons, pre-accelerated using a conventional accelerator cross the laser field in order to get, if possible, an energy boost. Although this has been a quite common experimental scenario, as we said,

we are not going to consider it. In this chapter we will refer only to independent electrons appearing from atoms or molecules after being suddenly ionized by barrier suppression.

8.2 Relativistic Modelling of Laser Driven Electrons

One of the reasons for the interest in the electron motion is its apparent simplicity: interaction of a charged particle with an electromagnetic field in vacuum. At low intensities, the classical motion of the electron is governed by the laser electric field. Beyond 10^{18} W/cm**²**, however, the laser field is so strong that dynamics becomes relativistic, and the coupling to the laser magnetic field is equally important for the motion description.

Motion is described by the Lorentz force, $\overrightarrow{F} = -e\ (\overrightarrow{E} + \vec{v} \times \overrightarrow{B}/c)$, where $\vec{v}$ indicates the speed of the electron and c is the speed of light. $\overrightarrow{E}$ and $\overrightarrow{B}$ are the electric and magnetic fields of the laser beam. We consider that the electron charge is -e (e being positive). Then the relativistic equation of motion is

$$\frac{d\overrightarrow{p}}{dt} = \overrightarrow{F} = -e\left(\overrightarrow{E} + \frac{\overrightarrow{v}}{c} \times \overrightarrow{B}\right) \tag{8.1}$$

where $\vec{p} = m\gamma\vec{v}$, is the momentum and $\gamma^{-1} = \sqrt{1 - v^2/c^2}$ is the well-known relativistic factor. And thus,

$$\frac{d}{dt}(\gamma\overrightarrow{v}) = -\frac{e}{m}\left(\overrightarrow{E} + \frac{\overrightarrow{v}}{c} \times \overrightarrow{B}\right) \tag{8.2}$$

The relativistic factor is the origin of interesting nonlinear effects, that will dominant as intensity increases.

The electron is a spin ½ fermion, so for high intensities there must be a coupling between the laser magnetic field and the spin. Fortunately, the free electron Dirac equation can be worked out analytically for the case of plane propagating pulses, regardless of the intensity [10]. When working with such huge electromagnetic fields it is reasonable to consider the coupling of the magnetic field with the electron spin. Nevertheless, it has been shown [11] that such coupling is extraordinarily small and can be neglected without introducing any relevant source of error. This justifies the use of a classical (non-quantum) description for the driven electron, and thus the validity of the motion at high intensities.

Probably the most limiting factor for the validity of the forthcoming calculations at ultra-high intensities is radiation reaction [12]. The onset for radiation reaction relevant effects, with a near infrared laser, occurs around 10^{23} W/cm^2. We are going to consider relativistic intensities always below that limit.

Therefore, a description based in the relativistic dynamics will be employed. In components, the Lorentz equation becomes:

$$\begin{aligned}
\frac{d}{dt}(\gamma\, v_x) &= -\frac{e}{m}\left(E_x + \frac{1}{c}\left(v_y\, B_z - v_z\, B_y\right)\right)\\
\frac{d}{dt}\left(\gamma\, v_y\right) &= -\frac{e}{m}\left(E_y + \frac{1}{c}\left(v_z\, B_x - v_x\, B_z\right)\right)\\
\frac{d}{dt}(\gamma\, v_z) &= -\frac{e}{m}\left(E_z + \frac{1}{c}\left(v_x\, B_y - v_y\, B_x\right)\right)
\end{aligned} \tag{8.3}$$

Plane wave analytical solution

For the particular case of a propagating plane wave, monochromatic or pulse, Sarachik and Schappert developed a very elegant and useful exact solution [13] that considers a propagating plane wave pulse of arbitrary shape. Their only condition is that the pulse profile function depends only on a variable $\eta = \vec{s} \cdot \vec{r} - c\,t$ where $\vec{s}$ is a unitary vector indicating the propagation direction. For simplicity we will define z as the propagation direction, and thus $\eta = z - c\,t$ gives the pulse shape. For an electron initially at rest, its energy is given by

$$E(\eta) = mc^2\left[1 + \frac{e^2 A^2(\eta) f^2(\eta)}{2m^2c^4}\right] \tag{8.4}$$

$\vec{A}(\eta)\, f(\eta)$ indicates the vector potential, where $f(\eta)$ is a normalized pulse envelope ($f = 1$ at its maximum) that accounts for the pulse profile of the $\vec{A}$ field. We consider that $\vec{A}$ is oscillating at a laser frequency ω and the pulse envelope function gives the bandwidth. Sarachik and Schappert showed also that the momentum is given by

$$\vec{p}(\eta) = -\frac{e}{c}\,\vec{A}(\eta)\, f(\eta) + \vec{s}\,\frac{e^2 A^2(\eta) f^2(\eta)}{2mc^3} \tag{8.5}$$

This expression is very relevant because it shows that the momentum has a transverse component (in the direction of polarization of the vector potential $\vec{A}$) and a longitudinal component (in the direction of the propagation $\vec{s}$). The electric field is related to the vector potential by the well-known relation $\vec{E} = -\left(1/c\right)\,\partial\vec{A}\Big/\partial\, t$. For a plane wave pulse therefore, the momentum has an exact analytical solution (fully relativistic) indicating its two components, one along the vector potential and the other along the propagation direction (z). The two components lie in the plane defined by $\vec{E}$ and $\vec{s}$. Their relation defines a characteristic angle that indicates the averaged motion direction of the electrons in the field. This motion is the first clear expression due to the ponderomotive force. The electron is forced to move forward due to this effect. Of course, it can't move faster than light and eventually ends behind the pulse.

For a linearly polarized plane wave laser field,

$$E_x = E_0\, f(z-ct)\cos(k(z-ct))$$
$$B_y = B_0\, f(z-ct)\cos(k(z-ct)) \tag{8.6}$$

the situation is shown schematically in Fig. 8.1, This motion is oscillatory and at the end the electron will return to rest (provided that initially it was at rest). The oscillation has some typical features. It has harmonic frequencies based on the fact that E_x accelerates the electron along x, and the corresponding velocity v_x couples with the B_y magnetic field giving a v_z speed. From E_x and B_y it is impossible to get acceleration along the direction of the magnetic field if initially the speed is zero, therefore the trajectory lies in the xz plane. The longitudinal component of the velocity can be quite large and therefore the Doppler shift is very relevant. This can be indirectly seen in Fig. 8.1 because the oscillation is much larger than the initial laser wavelength, marked as λ in the figure. Also, this schematic plot shows a very peculiar characteristic, the cusps. At those cusps the electric field gets its maximum value and the electron experiences the maximum acceleration. Such figure seen from a reference frame moving with the average speed of the electron presents a characteristic figure-of-eight pattern as studied in Sarachik and Shappert paper. More relevant is the fact the v_xB_y term couples two terms oscillating at the laser frequency, so it is going to generate a second harmonic and as a consequence many more harmonics. The oscillatory motion in a laser field becomes anharmonic [14] The pattern of frequencies generated by such relativistically driven electron is quite relevant for a number of applications [15, 16].

Computed electron trajectories, for a propagating plane wave laser field linearly polarized along the x-axis, are shown in Fig. 8.2. This is a numerical simulation but is totally in the region of validity of the analytical expressions of Sarachik and Shappert, and fits them well. The pulse envelope is $f(\eta) = \exp(-(\eta/c\,\tau)^2)$, with a time duration τ equal to 10 laser cycles. The figure corresponds therefore to a plane

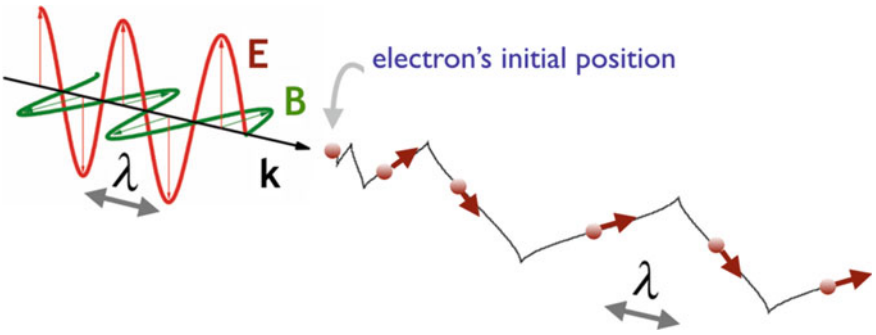

Fig. 8.1 Motion of an electron driven by a plane wave laser. Although this is just a scheme, it is quite realistic for an intensity of 2 10^{19} W/cm^2 and 800 nm wavelength

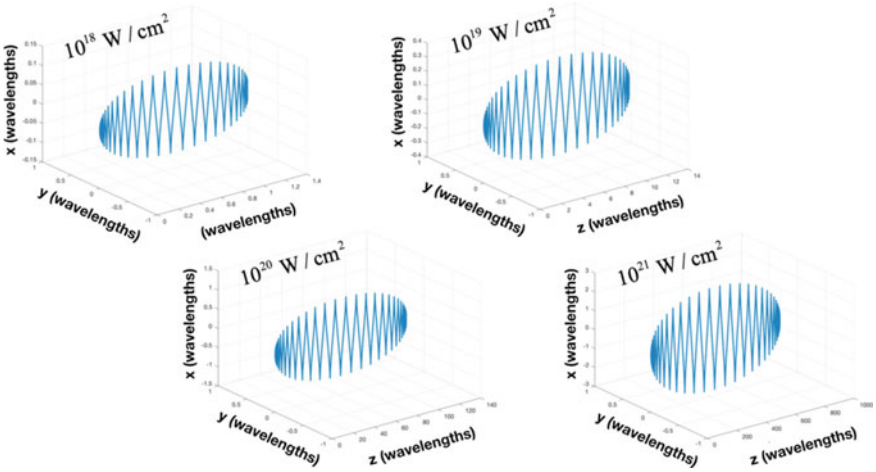

Fig. 8.2 Trajectories of a driven electron initially at rest at the origin of coordinates, in the situation of applicability of the Sarachik-Schappert analytical model. The central wavelength is 800 nm. It corresponds to a plane wave with the pulse envelope $f(\eta) = \exp(-(\eta/c\,\tau)^2)$, and τ equal to 10 laser cycles. The four trajectories correspond to different intensities, all in the relativistic domain. The electrical field is linearly polarized (only E_x component). Although this plot is a numerical computation, it agrees perfectly with their analytical result for plane waves

propagating wave, and four different peak fields are shown, with intensities from 10^{18} W/cm^2, that is the onset of the relativistic effects, to a strongly relativistic case10^{21} W/cm^2. Observe that the four plots look quite similar and only the spatial scales change. This is so because the number of oscillations corresponds to the number of laser periods. In all cases the forward drift (due to the forward ponderomotive force) is evident but its magnitude is quite different. In this case (plane wave) electrons are forced forward, but always at a speed less than c, and sooner or later have to cross the maximum of the field and slow down until the next maximum (or minimum) of the field. This effect is well known and has been described as electron slippage [17].

Initial conditions and ionization dynamics

The aim of this contribution is to show the relevance of the ponderomotive potential in realistic experimental situations of atoms or molecules interacting with intense laser pulses. If one is using an electron beam, then pre-accelerated electrons are there from the very beginning. However, in the atomic or molecular case we start with neutrals. Electrons do not feel the laser field until they are ionized.

In most of the calculations found in the literature, electrons are considered free from the very beginning, so they feel the turn-on of the pulse and they are subject to smooth dynamics that can bring considerations similar to the ones that originate the Lawson Woodward theorem [18, 19]. In the real situation we need a model for ionization, and this would depend on the atomic or molecular species. In the context of relativistic intensities, we can consider that electrons are released when the field

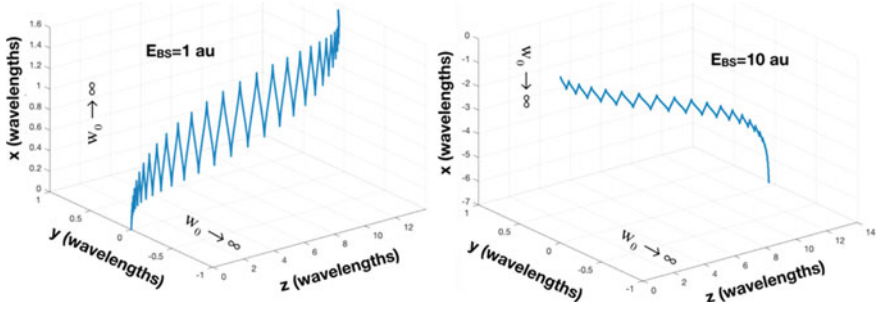

Fig. 8.3 Trajectories for a plane wave pulse for the same conditions as in the previous figure (plane wave 10 cycles long pulse) with intensity 10^{19} W/cm^2. While in the previous figure electron was free from the very beginning, now the electron is released suddenly when the laser field arrives to a given value, E_{BS}, to ionize by barrier suppression. The value $E_{BS} = 1$ a.u. (3.5 10^{16} W/cm^2). Observe the drift induced. This drift is much larger if the electron is released at higher fields as can be the case of inner electrons $E_{BS} = 10$ a.u. (3.5 10^{18} W/cm^2)

amplitude reaches the barrier suppression regime. Well above this barrier suppression field, in the region 10^{14} to 10^{15} W/cm^2 for valence electrons of most atoms, electrons are hundred percent ionized almost instantaneously. This simple model considers that electrons are frozen (inside the atoms or molecules) until the field reaches a given value high enough to fully ionize them. In other words, we wait until the laser field reaches a convenient value (we call this E_{BS}, from barrier suppression) and then the electron is released inside the field. This is not a minor point. To prove that we show in Fig. 8.3 the influence of E_{BS} on the electron's drift. This figure shows two individual trajectories for a plane wave pulse for the same conditions as Fig. 8.2 (10 cycles long pulse) with intensity 10^{19} W/cm^2. While in Fig. 8.2 the electron is free from the very beginning, in Fig. 8.3 the electron is released suddenly when the laser field arrives to a given value, E_{BS}, to ionize by barrier suppression. The value $E_{BS} = 1$ a.u., corresponding to an intensity 3.5 10^{16} W/cm^2 can be a realistic choice for complete ionization. Observe the drift induced, this drift is much larger if the electron is released at higher fields as can be the case of inner electrons, that can be simulated introducing a larger value of the barrier suppresion field, for example $E_{BS} = 10$ a.u. (3.5 10^{18} W/cm^2). This is quite relevant in the present context because the distribution of the released electrons after the pulse will be influenced by the moment where they appear. Inner shell electrons or second or third ionizations will have different transverse distributions in the end.

8.3 Paraxial Beams Close to Waist

An ultrafast ultraintense laser beam is typically a flat-top with some inhomogeneities that can be as large as 10 percent, in intensity. It is focused generally with an off-axis parabola mirror and generates a focal spot and a transverse distribution of intensity in

the focal plane. However, not all of the laser beam energy is concentrated on the focal spot due to the profile of the beam or spatial and temporal aberrations, and a fraction of it is lost. If the beam profile were an ideal flat top, the profile at the focal plane would be the well-known Airy pattern due to diffraction (Fraunhofer diffraction) by a circular aperture. Realistic modelling of the focus is now possible but depends on many parameters, a number of them unknown.

A widely used first approximation that represents a reasonable compromise between realistic description and simple mathematical model are paraxial beams. When focusing the pulse with a long focal, such an approximation is reasonable. Harmonic paraxial beams are solutions of the Helmholtz equation, k being the harmonic wavenumber, $\partial^2 \vec{E} \Big/ \partial\, x^2 + \partial^2 \vec{E} \Big/ \partial\, y^2 = -ik\partial \vec{E} \Big/ \partial\, z$. The problem is that the three components are not independent, they must obey the condition $\vec{\nabla} \cdot \vec{E} = 0$, this condition is fundamental to understand ponderomotive potentials, as we will show. Pulsed paraxial beams can be described with the introduction of a pulse function $f(\vec{r}, t)$, with a gaussian time dependence $\exp(-(t/c\tau)^2)$, τ being the pulse duration, as indicated above**.** Such pulse description is reasonable for pulses of 30 fs (for Ti:Sapphire) or longer. For a few cycles pulses some corrections have to be added. Other $f(\vec{r}, t)$ functions can be used that give a realistic description ($\sin^2$, sech, and more), but we are going to consider only the gaussian pulse shape. In fact we are going to consider only Ti:Sapphire 800 nm laser pulses, with a realistic pulse duration, $\tau = 10\, cycles$. This gives a reasonable descriptition of most of the existing high-field PW or multi-PW lasers around the world, including the Salamanca PW laser.

Hermite-Gauss or Laguerre–Gauss modes (depending on the symmetry we want to explicitly consider), give paraxial solutions of interest. These modes are widely studied in the literature and they are characterized by a waist w_0 and a Rayleigh length z_R, related by $z_R = \pi\, w_0/\lambda$. Their value depends on the F number of the focusing system. If we are close to focus, i.e. if the distance from focus is smaller than the Rayleigh length, wave-fronts are almost constant z planes and it is possible to describe the field in the form,

$$E_x = E_0 \exp\left(-\rho^2 \Big/ w_0^2\right)\, f(z - ct) \cos(k(z - c\, t)) \tag{8.7}$$

Paraxial gaussian beams give very nice and useful descriptions of the fields before and after the waist, including the corresponding spherically converging or diverging wavefront. The generalization to such beams is straight forward, but in the present notes we are going to consider that all wavefronts are planes perpendicular to z. This is reasonable only if we are close to the beam waist, the region where most experiments are performed. We introduce the name CTW (Close-to-Waist) approximation, to refer to this plane wavefront description that is valid just at a distance from the waist much smaller that the Rayleigh length. The big simplifying advantage to the CTW approximation is the fact that we have just a propagating beam. Propagation depends again only on the $\eta = z - c\, t$ variable and the comparison with the infinite plane analytical solutions is more evident. The CTW approximation represents a

nice compromise between a realistic model and a model that is simple enough to get compact expressions of the low order modes. Being close to the waist the Gouy phase has been neglected, however it can be included when a careful consideration of the phase velocity is needed because Gouy phase is a z-dependent phase to be added to the propagation. In the following discussion we neglect the Gouy phase and therefore we neglect the phase slippage it generates.

Scalar modes

The lowest order mode, the gaussian mode, is given by the scalar function,

$$u_{00}(\vec{r}) = u_0 \exp\left(-\rho^2/w_0^2\right) f(z-ct) \cos(kz-\omega t) \tag{8.8}$$

As is well known, the dependence of the next two modes is

$$\begin{aligned} u_{10}(\vec{r}) &= u_0 \frac{x}{w_0} \exp\left(-\rho^2/w_0^2\right) f(z-ct) \cos(kz-\omega t) \\ u_{01}(\vec{r}) &= u_0 \frac{y}{w_0} \exp\left(-\rho^2/w_0^2\right) f(z-ct) \cos(kz-\omega t) \end{aligned} \tag{8.9}$$

To describe more complicated transverse profiles, it is always possible to consider higher order Hermite-Gauss, or Laguerre–Gauss modes, depending of the transverse symmetry of the problem (circular or squared). It is also possible to consider geometries where the waist is not circular, but larger in one dimension that other. In that case one needs to replace the ρ^2/w_0^2 term in the exponential giving the transverse profile by $x^2/w_{0x}^2 + y^2/w_{0y}^2$, w_{0x} being the waist in the x direction and w_{0y} in the y direction (Fig. 8.4).

Clearly, the u_{10} scalar function has a node along the yz plane, while the u_{01} scalar function has a node along the xz plane. Adding these two modes in phase one gets a node plane at 45 degrees. However, adding them $\pi/2$ out of phase generates the simplest beams with one unit of OAM (Orbital Angular Momentum), i.e.

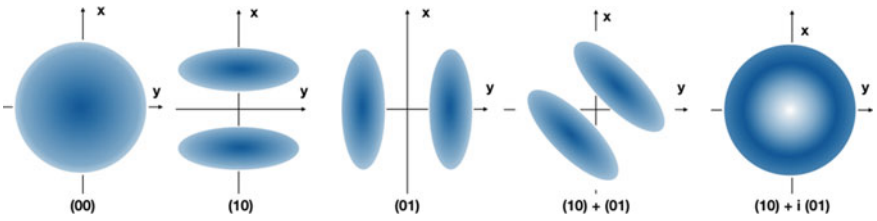

Fig. 8.4 Schematic representation of the amplitude distribution on the transverse plane of the different scalar modes. (00) indicates the u_{00} scalar function; (10) indicates the u_{10} scalar function; (01) indicates the u_{01} scalar function; (10) + (01) is the sum in phase of the two previous ones; and (10) + i(01) indicates the sum with a $\pi/2$ dephasing, that corresponds to u_1, the simplest mode with non-vanishing Orbital Angular Momentum

$$u_1(\vec{r}) = u_0 \ \exp\left(-\rho^2 / w_0^2\right) \ f(z-ct) \ \left(\frac{x}{w_0}\cos(kz-\omega t) + \frac{y}{w_0}\sin(kz-\omega t)\right) \tag{8.10}$$

Vector transverse modes

Those three basic scalar modes, (00), (01) and (10), are enough to get a clear description of the relativistic ponderomotive force. To calculate the trajectory of the electron it is necessary to take a full vector description of the fields, taking also into account the longitudinal fields to fulfill the $\vec{\nabla}\cdot\vec{E} = \vec{\nabla}\cdot\vec{B} = 0$ transversality conditions both for electric and magnetic fields.

For the rest of this chapter we are going to study five of such vectorial modes, that represent modes with internal structure able to generate different dynamics. Most of the ponderomotive potential relevant features can be obtained using these basic modes and combinations of them with convenient phases and/or delays.

Gas density

In the simulations we consider a dilute neutral gas from which electrons appear. The gas density is assumed to be low enough to not modify the laser propagation indicated in Eqs. (8.8) and (8.9). Ionized electron density is assumed also to be small enough to not affect the propagation. In other words, the refractive index (linear and nonlinear) induced by the neutrals, the ions and the ionized electrons is not relevant to change the fields propagation. In our model, moreover, electrons move independently, without interacting between them.

All this can be realistic for Argon, Nitrogen or other gases at low pressures (from 10^{-2} to 10^{-4} mb) and for slightly higher pressures for the case of Helium. Higher densities would imply B integral effects and collisions and the present model will fails. In the collision dominated regime PIC simulations are needed [20].

8.4 Numerical Results for the Lowest Order Mode

Our purpose is to give the reader some degree of intuition about the ponderomotive force that can be useful for the design of high field experiments where relativistic or ultra-relativistic dynamics is dominant. We will present several mode combinations that induce conceptually different ponderomotive patterns.

We start with the simplest mode, the gaussian (00) mode. Because we are going to introduce different polarizations, we introduce a compact notation, labeling this mode as ($\times$00), where x stands for the polarization (electric field in the xz plane) and 00 indicates the mode. The gaussian mode, linearly polarized along x, can be written as:

$$
\begin{aligned}
E_x &= E_0 \exp\left(-\rho^2/w_0^2\right)\ f(z-ct)\cos(kz-\omega t) \\
E_z &= E_0 \exp\left(-\rho^2/w_0^2\right)\ f(z-ct)\ \ \sin(kz-\omega t)\ \frac{2\,x}{w_0}\,\frac{1}{k w_0} \\
B_y &= B_0 \exp\left(-\rho^2/w_0^2\right)\ f(z-ct)\cos(kz-\omega t) \\
B_z &= B_0 \exp\left(-\rho^2/w_0^2\right)\ f(z-ct)\ \ \sin(kz-\omega t)\ \frac{2\,y}{w_0}\,\frac{1}{k w_0}
\end{aligned}
\tag{8.11}
$$

With $E_y = 0$, and $B_x = 0$. Observe that in the E_z and B_z expressions we neglected the space derivative of the pulse profile function f. This can be reasonable in the context of the rest of the approximations made provided that the pulse is not too short. Observe thus that there are two large components, E_x and B_y, and two small longitudinal components E_z and B_z introduced to keep the transversality in the CTW region. The $1/kw_0$ factor gives a reference for the relative size of the longitudinal field. To be consistent, the error introduced when neglecting the z derivative of the pulse shape function f must be much smaller. Although it is well known, it is always convenient to remember that in spite of its small value (even when $kw_0 << 1$) the longitudinal field is fundamental for a proper description of the ponderomotive dynamics [21].

As is well known, within the CTW approximation, the longitudinal components are in quadrature with the transverse components (in our case, considering just the real fields for simplicity, this means that the phase dependence is $\cos(kz-\omega t)$ for the transverse components and $\sin(kz-\omega t)$ for the longitudinal ones). To understand this, it is convenient to write explicitly the components of the Lorentz equation,

Without transverse fields

$$
\left.
\begin{aligned}
\frac{d(\gamma\, v_x)}{dt} &= -\frac{e}{m}E_x + \frac{e}{mc}v_z\, B_y \\
\frac{d\left(\gamma\, v_y\right)}{dt} &= 0 \\
\frac{d(\gamma\, v_z)}{dt} &= -\frac{e}{mc}v_x\, B_y
\end{aligned}
\right\}
$$

With transverse fields

$$
\left\{
\begin{aligned}
\frac{d(\gamma\, v_x)}{dt} &= -\frac{e}{m}E_x - \frac{e}{mc}v_y\, B_z + \frac{e}{mc}v_z\, B_y \\
\frac{d\left(\gamma\, v_y\right)}{dt} &= +\frac{e}{mc}v_x\, B_z \\
\frac{d(\gamma\, v_z)}{dt} &= -\frac{e}{m}E_z - \frac{e}{mc}v_x\, B_y
\end{aligned}
\right.
\tag{8.12}
$$

We can observe that without the longitudinal fields, and when the electron is initially at rest, the motion is in the xz plane. The ponderomotive displacement along the y axis requires the longitudinal magnetic field.

The best way to show the essence of the ponderomotive force is to consider a gaussian 00 mode. In the next figures we show snapshots of the motion of the barrier suppression ionized electrons driven by such a field mode (Fig. 8.5).

We consider a cloud of 10^4 electrons originally randomly distributed over a transverse region of $\pm\, x_{max}$ by $\pm\, y_{max}$. They are placed in the slab $0 < z < 10\,\lambda$. Using a thicker z slab does not add relevant information and at the same time blurs the results. The transverse size, $2x_{max}$ by $2y_{max}$, is chosen in order to span the whole range of

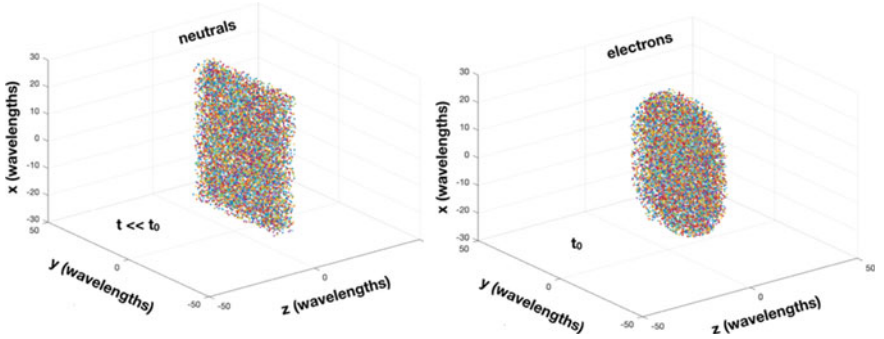

Fig. 8.5 Typical example of the initial cloud of 10^4 points considered in the numerical simulations. Left) Those points represent neutral atoms able to release one electron when the field amplitude reaches a given value, chosen as E = 1 au in the present plot. This is an arbitrary but reasonable value. The profile is a parallelogram of 10 wavelengths in the longitudinal direction (from $z = 0$ to $z = 8\,\mu m$) and enough spreading in the transverse plane to account for all atoms that can be ionized. The initial density of points is uniform. Right) After the arrival of the (×00) pulse ionized electrons appear and start moving. The figure on the right depicts only the ionized electron cloud

transverse positions where the electron can appear by barrier suppression ionization. For a (00) pulse, the maximum transverse radius, $\rho_{\max}$, at which electrons are born, is given by $\rho_{\max} = w_0 \sqrt{\ln\left(E_0 / E_{BS}\right)}$. For other combinations of pulses this may vary. In the simulations we guarantee that the random sampling homogeneously covers the region where electrons can appear (i.e. the region with field higher that E_{BS}).

The number of electron trajectories used in our simulations has nothing to do with the actual gas density in an experiment. The number of computed trajectories has to be large enough to get a visual idea of the electron cloud motion. The gas density can be increased up to the point where collective effects become relevant and this is several orders of magnitude above the density of trajectories considered.

The situation to be described in the following simulations is shown in Fig. 8.6. Some of the mode configurations to be analyzed will have an offset Δ. In the combinations involving the (00) mode, it will be the delayed one. In a real experiment the cloud of atoms from a jet nozzle will be very thick, however we consider that the atoms are localized only in the space between the z = 0, and the z = 8 microns planes. Due to the CTW approximation, the consideration of a thicker electron cloud will be simply a repetition of that. To be sure that the initial dynamics is properly accounted for, we consider that at the starting of the computation we have just neutral atoms. Being precise, we start the computation at a time when the pulse envelope function $E_0 f(z - ct) << E_{BS}$. In order to have a clear reference of the time scale for each of the following plots, we define a time t_0 as the time when the maximum of the first component arrives to z = 0 (i.e. $f(ct_0) = 1$). All figures and discussions will be referred to this time. In the case of an offset Δ (for combinations of the gaussian modes with others) the maximum of the gaussian pulse will arrive to z = 0 at time $t_0 + \Delta/c$. Obviously t_0 has nothing to do with the time where the simulation started

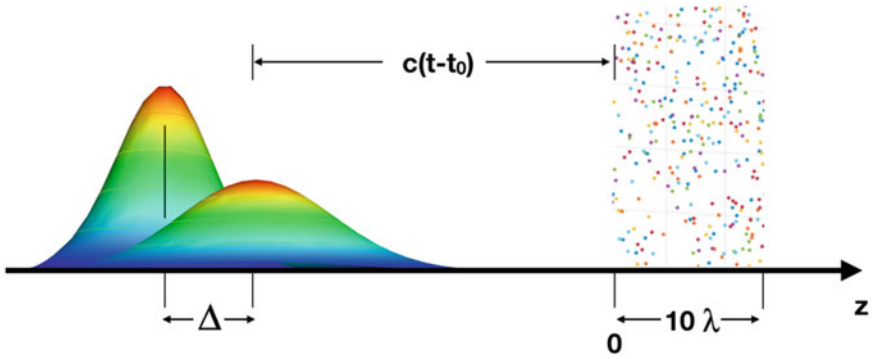

Fig. 8.6 Schematic representation of the initial situation. Randomly distributed neutral atoms (represented as dots) are waiting for the arrival of the pulse in a region 10 lambda thick. When field amplitude arrives to the barrier suppression value, E_{BS}, the atom at that point is ionized, i.e. the electron escapes from the atom/ion and starts moving. Δ is the offset of the (01) and (10), or their combinations. Typically we consider $\Delta = c\,\tau$ or $\Delta = c\,\tau/2$, to get interesting superpositions of intensity. This is just a scheme of the two pulses, of course, in the actual case they will interfere

that, depending on the parameters, particularly on the intensity, can be 20 or mode cycles before.

A simple "well known" case

Just to understand well the transition from plane propagating wave to a real case, we may consider the case of a large waist, 100 wavelengths (80 microns) and an intensity of 10^{19} W/cm^2 ($E_0 = 17$ au). Observe that this may seem a modest intensity however, considering that the waist is quite large this would correspond to about 100 TW of power. Power precisely inside the focal spot, not in other parts of the focal plane. This requires a very good beam quality plus a very high intensity, almost in the limit of today's lasers (Fig. 8.7).

Forward velocity mapping

Depicting electron trajectories, or electron clouds, in space gives direct information on the dynamics but gives an information that is difficult to see in a real experiment. In a number of experiments, it could be possible to measure the signature of the electron trajectories going out of the focal spot driven away by the ponderomotive force by analyzing the angles were electrons are to be found. We computed also the x and y directions, i.e. we plot v_x/v_z and v_y/v_z (v_z being the longitudinal speed), so those plots give the integrated forward pattern of the electron ponderomotive explosion. In principle this could be measured with a scintillator or a radio-chromic plate strategically placed after the focal spot. Although in those cases one would get the integrated pattern, it is also interesting to analyze (but much more difficult to observe) its time evolution because at the beginning, as shown in Fig. 8.8, dynamics is dominated by the $v_x B_y$ term, as in Sarachik-Shappert analytical theory, and the motion is along the electric field polarization. When the v_x velocity combines with

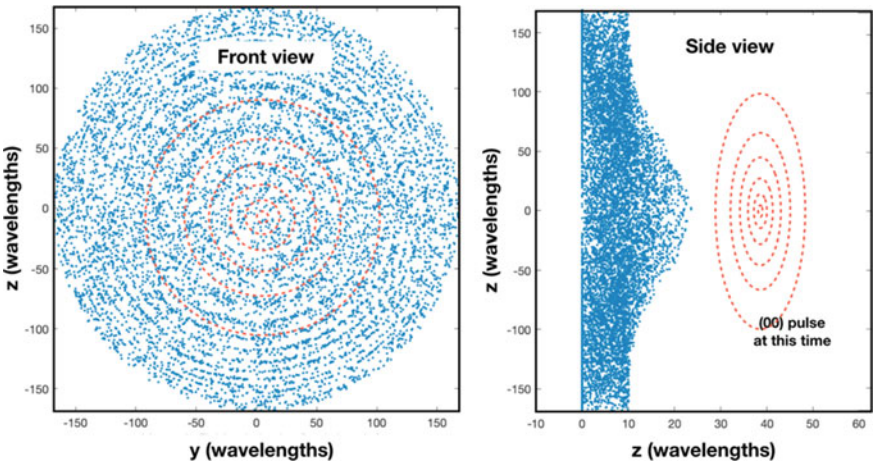

Fig. 8.7 Representation of the position of the electrons just after the pulse, for a large waist (oblate gaussian pulse with waist $w_0 = 100$ wavelengths, and duration 10 cycles) for 10^{19} W/cm^2 ($E_0 = 17$ au). The front view shows the transverse plane (plane xy). The side view shows the y axis projection. Both correspond to the final position of those electrons after the pulse. Dashed lines indicate the pulse contour (the outer one corresponds to 1/e amplitude, i.e. its radius is w_0)

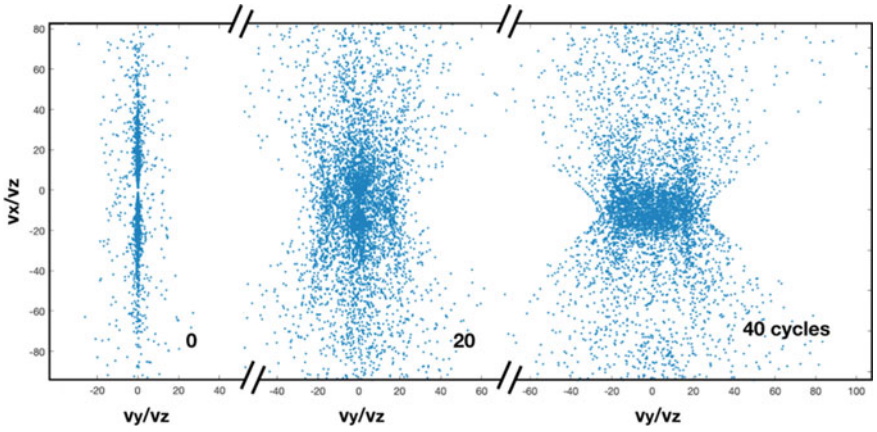

Fig. 8.8 Evolution of the dynamical pattern. Initially the dynamics is driven by the v_xB_y term, as in the Sarachik-Shappert analytical description, later the longitudinal field drives the electron. All parameters as in Fig. 8.7, including the 80 μm beam waist

the longitudinal field we start to have ponderomotive repulsion along the y axis too. This process needs a time because the longitudinal component of the electric field is zero along the $x = 0$ plane and the longitudinal component of the magnetic field is zero along the $y = 0$ plane.

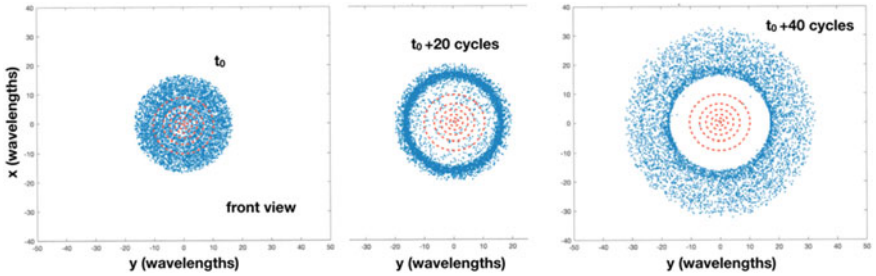

Fig. 8.9 Front views of the distribution for the (×00) mode, for a mildly relativisitic field, Eo = 17 a.u. (10^{19} W/cm^2), spherical pulse ($w_0 = c\tau = 10\lambda = 8\,\mu m$). Time t_0 corresponds to the moment where the maximum of the gaussian pulse arrives to z = 0. The other plots correspond to 20 and 40 cycles later. Dashed lines indicate the pulse contour (the outer one corresponds to 1/e amplitude)

A large waist is closer to Sarachik-Shappert plane wave modelling. In Fig. 8.8 this can be seen, particularly analyzing the direction of the electronic motion. The plot shows the forward angles in the x and y directions (in fact shows the forward velocity tangents v_x/v_z and v_y/v_z). This plot is very interesting because at the beginning the distribution follows the motion in along the xz plane (v_y velocity is very small), but after 40 laser cycles transverse fields wash out the plane dynamics.

The ponderomotive pattern created by a (00) mode is well known. It is shown for the realistic case of an 8 μm waist in Fig. 8.9. This value of the waist will be the same for all the remainding plots in this chapter. The plot at the left, t_0, corresponds to the moment where the peak of the pulse arrives to z = 0 (electrons are, as indicated in Fig. 8.6, filling the region $0 < z < 10\lambda$). Calculations, however started a few tens of cycles before to guarantee that the field is well below barrier supression at the beginning of the computation. The time lapse between each of the three views is 20 cycles. On the right-hand side one the interaction with the pulse is over (the forward drift is small) and the ponderomotive explosion is clearly seen showing a region at the center empty of electrons. Some of those structures may look like as a shock wave, but they are not. Electron–electron repulsion is not accounted for and there are no collective plasma effects. The wave is a caustic of the different electronic trajectories. At higher intensities the dynamics is similar, electrons are pushed outwards and the central region is depleted quickly.

As a partial conclusion of this section, we just can say that the ponderomotive force for a convex pulse acts just as a repulsive force, expelling electrons out of the high intensity region, as expected. Nothing is new here, but these ideas are very relevant for comparison with higher order modes, with nodal planes or axial nodes, that will lead to a different dynamical phenomenology.

8.5 Numerical Results for the 10 or 01 Modes

The scalar modes (01) and (10) are very relevant because they represent a field with a nodal plane. Such nodal plane represents a minimum in in the ponderomotive potential and could deviate or trap electrons. When considering the vector modes, polarization can go along or be perpendicular to the nodal plane, therefore there are four basic modes, ($\times$01), ($\times$10), (y01), and (y10), according to the polarization of the electric field, as indicated in Fig. 8.10. We need to study all four modes because we are going to present some interesting combinations of them with the ($\times$00) gaussian mode. It is relevant to write them explicitly, including the longitudinal component.

In the equations for the different modes, we keep the E_0 amplitude, as we did with the gaussian pulse. However, while for the gaussian pulse E_0 indicates the maximum of the peak (at the center) with a 01 or 10 mode this is not. Because of the nodal plane, the maximum field occurs at a distance 0.7 w_0 (the exact factor is $1/\sqrt{2}$) of the node, and that peak value is $E_{max} = 0.43\ E_0$ (the exact factor is $\exp(-1/2)/\sqrt{2}$). Observe that intensities of those modes are calculated from E_{max} not from E_0.

Mode 10 with x polarization, ($\times$10)

The 10 mode, linearly polarized along x is:

$$\begin{aligned}
E_x &= E_0 \exp\left(-\rho^2/w_0^2\right)\ f(z-ct)\ \cos(kz-\omega t)\ \frac{x}{w_0} \\
E_z &= E_0 \exp\left(-\rho^2/w_0^2\right)\ f(z-ct)\ \sin(kz-\omega t)\ \left(\frac{2x^2}{w_0^2}-1\right)\frac{1}{kw_0} \\
B_y &= B_0 \exp\left(-\rho^2/w_0^2\right)\ f(z-ct)\ \cos(kz-\omega t)\ \frac{x}{w_0} \\
B_z &= B_0 \exp\left(-\rho^2/w_0^2\right)\ f(z-ct)\ \sin(kz-\omega t)\ \frac{2xy}{w_0^2}\frac{1}{kw_0}
\end{aligned} \tag{8.13}$$

The other two components are $E_y = B_y = 0$. The kw_0 inverse dependence in E_z and B_z is kept expicitely because this factor gives idea of the relative value of the

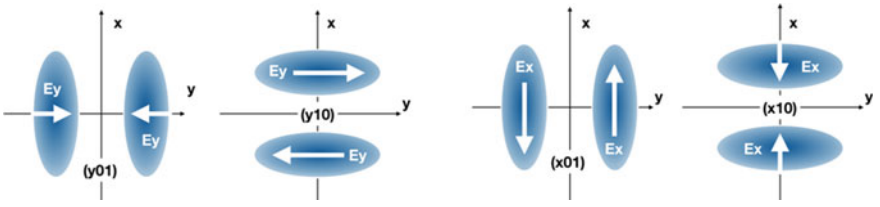

Fig. 8.10 Schematic representation of the four basic modes with one plane node. The four modes are relevant for this paper because we are going to present combined results with the linearly polarized gaussian mode

longitudinal fields. Again, in these expressions we have neglected the z derivatives of the pulse shape function f. Although this would be beyond the scope of the present paper, it is possible to develop these expressions with higher accuracy observing that we have odd and even degree polynomials of x and y. A complete description of those higher orders can be found in [22].

Pulses with a nodal plane are very interesting because the ponderomotive force traps electrons. Within a region of about $w_0/2$ from the nodal plane, the intensity gradient drives the electrons towards the nodal plane, we can consider this as the attraction basin for the nodal plane. Therefore, some electrons are trapped along the x axis in this case (x axis because is a 10 mode, not because of the polarization) and they propagate along the nodal plane. Ponderomotive expansion in the perpendicular direction takes place, as expected. This is clear in Fig. 8.11, that corresponds to a mildly relativistic case, $E_0 = 34$ a.u. (this corresponds to a maximum field of 7.5 10^{10} V/cm, i.e. to a peak intensity of 7.4 10^{18} W/cm^2). The snapshot is taken 45 cycles after the maximum of the pulse crosses the $z = 0$ plane. The side view at the right of this figure shows also the pulse profile (dashed lines). At the time shown, all electrons (initially in the $0 < z < 10\lambda$ slab) lie behind the laser pulse. The results show some tansverse trapping, as expected. The situation changes for strongly relativisitic pulses. Figure 8.12, is similar to the previous one, but now the intensity is 100 times more, i.e. it corresponds to a strongly relativistic case (7.4 10^{20} W/cm^2). Now the trapping is accompanied by a forward acceleration of the electron cloud. An electron eactly at the nodal plane will not feel any transverse field and will pass through the pulse. However, most of the electrons in the attraction basin experience a field that is quite intense. As those electrons bounce back from one side to the other of the nodal plane they experience a field that causes them to drift in the forward direction. The subsequent Doppler shift, makes them experience a longer wavelength field (in their moving frame) and the combined result is that electrons are drifted when trapped. As a consequence they do not go through the nodal plane. They stay for quite a large number of oscillations with the forefront of the pulse.

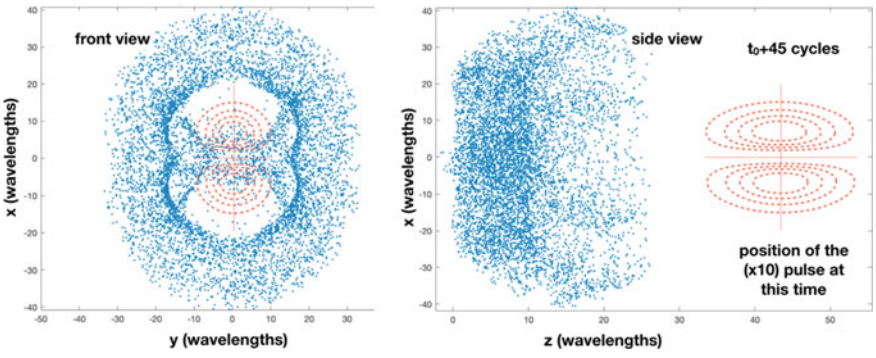

Fig. 8.11 Front view and side view of the electron distribution for a mode (×10) pulse with a mildly relativistic intensity, $E_0 = 34$ au. The pulse at the instant of the plot has already left all electrons behind. Dashed red lines show the pulse position at that time

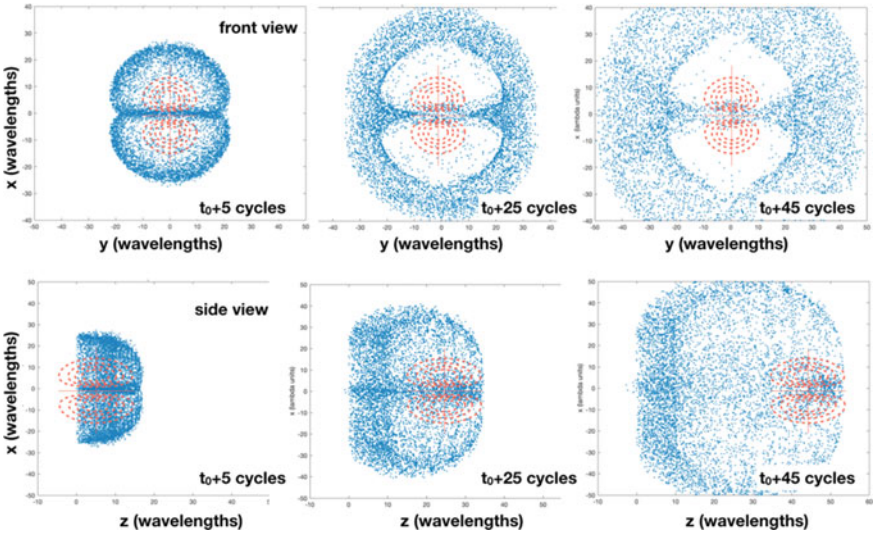

Fig. 8.12 Mode (×10) for a high intensity. The upper plots show the front view of the electron cloud and the lower ones the side view. There is trapping along the mode 01 node. The amplitude is $E_0 = 340$ a.u. (7.4 10^{20} W/cm^2). In this case, the quivering motion due to the electric field is perpendicular to the nodal plane

The simulation shown in Fig. 8.12 indicates a trapping ponderomotive force in one direction and a repulsive motion in the other. In other words, the ponderomotive potential has a saddle point. For that reason, electrons are trapped along the x axis but escape along the y.

Mode 10 with y polarization, (y10)

The 10 mode, linearly polarized along y is:

$$\begin{aligned}
E_y &= E_0 \exp\left(-\rho^2/w_0^2\right) f(z-ct)\ \cos(kz-\omega t)\ \frac{x}{w_0} \\
E_z &= E_0 \exp\left(-\rho^2/w_0^2\right) f(z-ct)\ \sin(kz-\omega t)\ \frac{2xy}{w_0^2}\frac{1}{kw_0} \\
B_x &= -B_0 \exp\left(-\rho^2/w_0^2\right) f(z-ct)\ \cos(kz-\omega t)\ \frac{x}{w_0} \\
B_z &= -B_0 \exp\left(-\rho^2/w_0^2\right) f(z-ct)\ \sin(kz-\omega t)\ \left(\frac{2x^2}{w_0^2} - 1\right)\frac{1}{kw_0}
\end{aligned} \tag{8.14}$$

The other two components are are $E_x = B_y = 0$. There is no need to show specific plots for this case because they are quite similar to the ones shown in Fig. 8.12, trapping along the x axis is due the mode (10) amplitude profile, not to the field polarization. However, in this case the electric field is driving the electrons along the nodal plane, not across it, as in the previous case. The remaining two modes will

have the same ponderomotive characteristics. We write them explicitly, just to have they expressions for the next sections, although they are only rotations.

Mode 01 with x polarization, (×01)

The 01 mode, linearly polarized along x, is

$$\begin{aligned}
E_x &= E_0 \exp\left(-\rho^2/w_0^2\right)\ f(z-ct)\ \cos(kz-\omega t)\ \frac{y}{w_0} \\
E_z &= E_0 \exp\left(-\rho^2/w_0^2\right)\ f(z-ct)\ \sin(kz-\omega t)\frac{2xy}{w_0^2}\ \frac{1}{kw_0} \\
B_y &= B_0 \exp\left(-\rho^2/w_0^2\right)\ f(z-ct)\ \cos(kz-\omega t)\ \frac{y}{w_0} \\
B_z &= B_0 \exp\left(-\rho^2/w_0^2\right)\ f(z-ct)\ \sin(kz-\omega t)\ \left(\frac{2\,y^2}{w_0^2}\ -1\right)\frac{1}{kw_0}
\end{aligned} \tag{8.15}$$

The other two components are. are $E_y = B_x = 0$.

Mode 01 with y polarization, (y01)

The 01 mode, linearly polarized along y, is

$$\begin{aligned}
E_y &= \ E_0 \exp\left(-\rho^2/w_0^2\right)\ f(z-ct)\ \cos(kz-\omega t)\ \frac{y}{w_0} \\
E_z &= E_0 \exp\left(-\rho^2/w_0^2\right)\ f(z-ct)\ \sin(kz-\omega t)\ \left(\frac{2\,y^2}{w_0^2}\ -1\right)\frac{1}{kw_0} \\
B_x &= -B_0 \exp\left(-\rho^2/w_0^2\right)\ f(z-ct)\ \cos(kz-\omega t)\ \frac{y}{w_0} \\
B_z &= -B_0 \exp\left(-\rho^2/w_0^2\right)\ f(z-ct)\ \sin(kz-\omega t)\ \frac{2xy}{w_0^2}\frac{1}{kw_0}
\end{aligned} \tag{8.16}$$

The other two components are $E_x = B_y = 0$.

In the next pages we are going to show simulations of the ponderomotive force induced by some of these modes as well as some combinations of them, with different delays and amplitudes. For simplicity, in all cases we are going to consider the Ti:sapphire wavelength, 800 nm, a beam waist $w_0 = 8\ \mu m$ and a pulse length $\tau =$ 10 cycles. There will be some delays between them, so we will indicate it as delay, for simplicity the gaussian 00 will be the reference and the other mode will come before (in these notes we are going to present only simulations where the 00 is the last one to arrive to the target). The offset or delay between one and the other will be on the order of the pulse duration or half of the pulse duration to have a clear interplay between them. For simplicity we can borrow the quantum mechanics notation of states (using parenthesis instead of brackets), so we are going to have combinations of the form $(\times 00) + a(y10) + b(y01) + c(\times 01) + d(\times 10)$, where a, b, c, d are complex numbers

giving the relative amplitudes and phases of the modes. The offset will be explicitly indicated for each example.

8.6 Numerical Results for Modes with an Axial Node (Donut Modes)

We saw that (10) or (10) modes trap in one dimension only. Therefore, as pointed out by Moore, convenient combinations of them will trap in the transverse plane. In other words, the three-dimensional saddle point will be attractive along the two transverse directions and repulsive along the forward axis. Taking into account the polarizations there are two conceptually different combinations, the standard donut mode mixing two crossed polarizations (and resulting -due to the lack of interference- as a flat-phase mode) and the OAM donut mode (mixing the same polarizations with a $\pi/2$ dephasing (resulting in a helical-phase mode).

Flat-phase donut mode

The more famous combination of those modes is the so-called donut mode. We can make such a mode with equal amplitude combinations of the ($\times$10) and (y01) modes or, alternatively with (y01) and ($\times$10). Regardless of the relative phase among them the mode intensity profile will have the well-known shape. Obviously, different phases between these two modes will result in different field patterns (radial polarization, for example), but the intensity profile is the same because being of crossed polarizations they do not interfere [23].

The idea of confining electrons at the center of an intense laser beam via the ponderomotive potential was suggested initially by Phillips and Sanderson [24] in a very preliminary form and later reexamined by Moore [25] for feasible laser conditions. As was pointed out by Moore such an axial node generates a tunnel that traps electrons in the transverse directions. Electrons born within a cylinder of radius approximately $w_0/2$ can be trapped. Figure 8.13 shows the numerical result for such donut mode ($\times$01) + (y10). Both plots correspond to the transverse projection of the electron cloud (x corresponds to the electric field polarization and z is the propagation). The left plot corresponds to a mildly relativistic case, $E_0 = 34 + 34$ a.u. (or 7.4 10^{18} W/cm^2 peak intensity for each mode), on each of the two modes. It is clear that some electrons went through the ponderomotive potential tunnel, but they are not pushed forward. The center of the donut pulse is at $z = 45\,\lambda$ for the left figure. The right plot corresponds to an intensity hundred times larger, $E_0 = 340 + 340$ a.u. (peak intensity 7.4 10^{20} W/cm^2 for each mode) and the picture corresponds to the time where the center of the donut pulse is at $z = 85\,\lambda$. Here the electron cloud evolution is completely different, the transversally trapped electrons feel a strongly relativistic field with the corresponding forward drift. The cloud of fast forward moving electrons is evident and it is still being pushed forward before the pulse maximum. Thus, at strongly relativistic intensities we can say that besides transverse trapping there is a

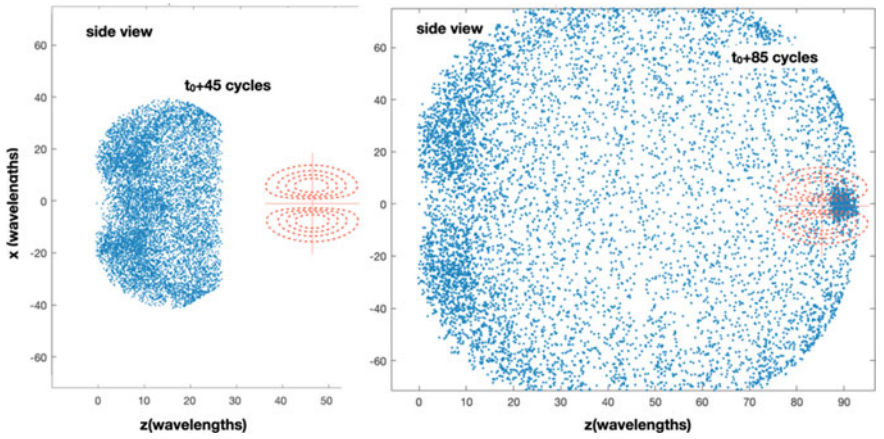

Fig. 8.13 Numerical result for the donut mode (×01) + (y10). Both plots correspond to the lateral projection of the electron cloud The left plot corresponds to an amplitude $E_0 = 34 + 34$ a.u., on each of the two modes (i.e. 7.4 10^{18} W/cm^2 each), and a time $t_0 + 45$ cycles, at that time the electron cloud is behind the pulse (the pulse position is indicated by the red dashed lines). The right plot corresponds to an intensity hundred times larger, $E_0 = 340 + 340$ a.u. (7.4 10^{20} W/cm^2) and to a time $t_0 + 85$ cycles. A number of trapped electrons have a strong drift forward, following the pulse

strong longitudinal drift that acts as a forward trapping. This effect was shown by Miyazaki and co-workers [26], but using an electron injector, instead of a gas of neutral atoms to be ionized. A similar effect will appear for the $l = 1$ OAM mode, because the ponderomotive force pattern is quite similar.

Helical-phase donut mode- (OAM mode, with parallel polarizations)

Combinations such as (×10) and (×01) are also quite interesting. Since both have the same polarization, their relative phase is very important. If both modes are in phase, i.e. combinations as (×01) + (×10), then we just shift the nodal plane and get just a rotation of ponderomotive potential pattern. However, if we introduce a $\pi/2$ phase shift among them, i.e. combinations of the form (×01) + i(×10), then we obtain an OAM $l = 1$ mode [27]. Such a mode has an intensity profile that looks like a donut mode, and it is called as donut many times in the literature. However, it has a helical phase structure. To avoid confusions, we will use the name donut to refer to the flat phase and OAM to refer to the helical phase $l = 1$ mode in this text. Observe that the helical structure of the OAM is in the phase distribution, the field polarization is always in the same direction (except, of course, the longitudinal component). Such Helical OAM modes can efficiently be produced form a (00) mode [28] using simple spiral staircase mirrors. This technique can be used in high intensity laser systems [29]. As a consequence, ultraintense OAM modes are achievable with existing lasers, and their potential for trap electrons in conjunction with other LWFA mechanisms has probably not being fully studied.

The in phase superposition of the (×01) and (×10) modes shifts the node to the $x + y =$ constant plane, however the superposition with a phase shift of $\pi/2$, gives

rise to the well-known OAM mode (with one unit of orbital angular momentum). The other possibility of combining two modes, y01 and y10 is just a rotation and does not add new information.

Figure 8.14 (upper part) shows the OAM mode ($\times 01$) + i($\times 10$) trapping, for E_0 = 34 + 34 a.u., i.e. a mildly relativistic case (7.4 10^{18} W/cm^2 at each component). Electrons are trapped in the minimum, but they are not pushed forward, so at the end there is a cloud of electrons repelled outwards by the ponderomotive force and a number of electrons trapped close to the axis. However, all electrons are out of the high intensity region, as can be seen in the upper right plot in Fig. 8.14. The lower part of Fig. 8.14 shows a case 100 times more intense. Transverse trapping perpendicularly to the beam axis is clear in this front view. However, there is a fundamental difference between them. For the strongly relativistic regime, electrons are pushed forward, so there is the expected trapping plus a relevant drift. This drift is evident in Fig. 8.14.

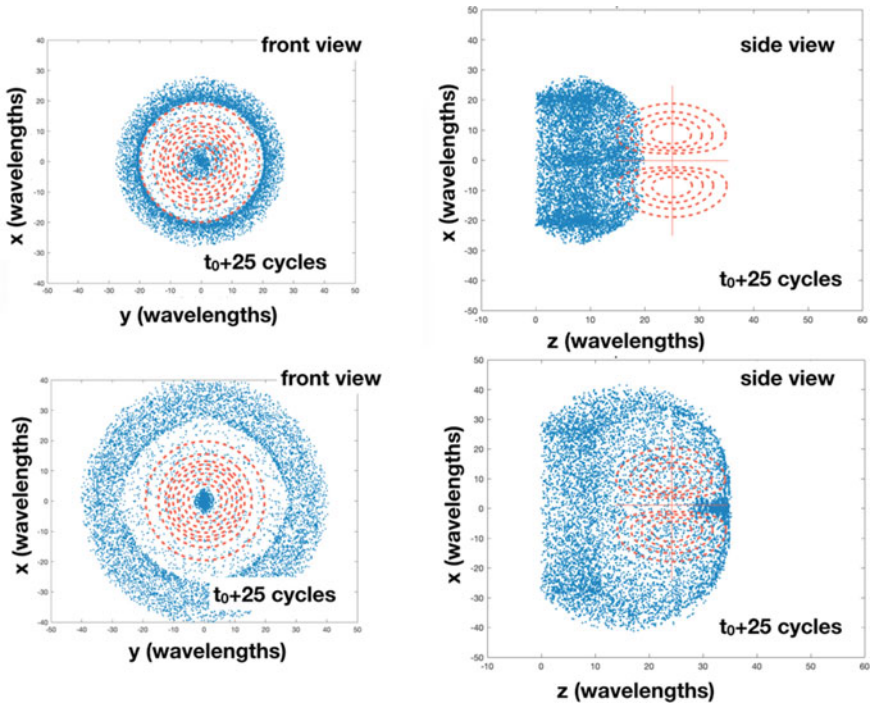

Fig. 8.14 Characteristic distribution of the electron cloud for an OAM, ($\times 01$) + i($\times 10$) of the electron distribution. The two upper figures are the front view and the side view for a mildly relativistic case, with amplitudes E_0 = 34 au (7.4 10^{18} W/cm^2). for each of the two modes. Result seems obvious, and is plotted just for comparison. The two lower plots correspond to the pulse structure but 100 times more intense, E_0 = 340 + 340 a.u. (7.4 10^{20} W/cm^2). In this case, a fraction of the electrons are also trapped in the axial node, but in this case they experience a strong drift forward. Time is 25 cycles after t_0

The OAM mode (×01) + i(×10) traps and drags a number of electrons when the intensity is strongly relativistic. Figures 8.15 and 8.16 correspond to the case E_0 = 340 + 340 a.u. (7.4 10^{20} W/cm^2 at each component) and evidence the electron

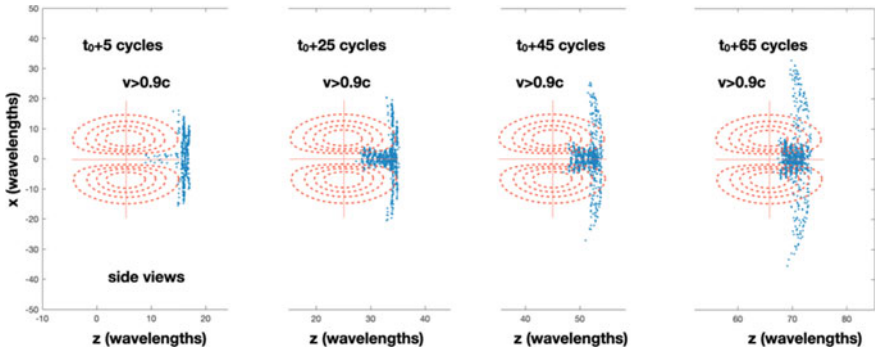

Fig. 8.15 Motion of the electronic cloud for a highly relativistic OAM mode, the same mode and fields as the previous figure. In the present plot only electrons with speed v > 0.9c have been plotted. The presence of a number of electrons close to the axial node and having a large drift is clear. Dashed lines indicate the position of the laser pulse

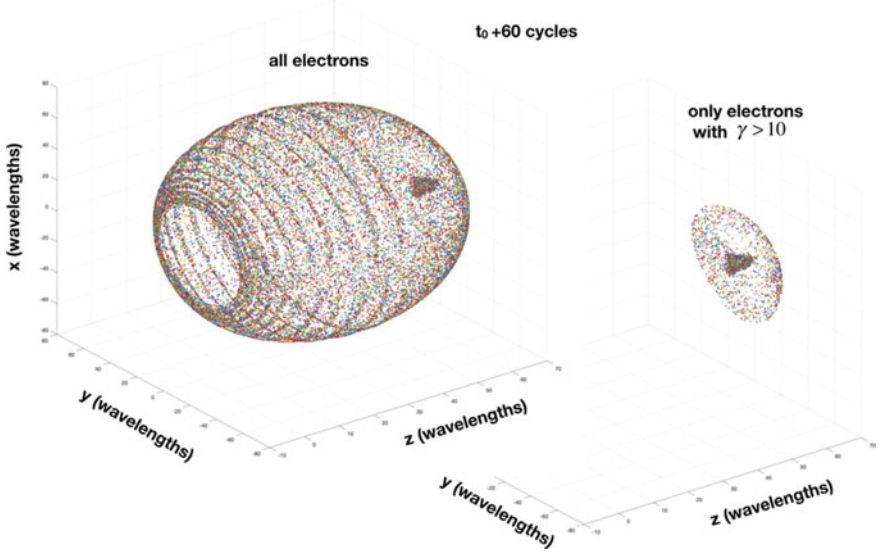

Fig. 8.16 Distribution of electrons at t_0 + 60 cycles. For a OAM mode (×01) + i(×10) with E_0 = 340 + 340 a.u. (7.4 10^{20} W/cm^2), and a waist w_0 equal to ten wavelengths, as in the previous figure. The left plot shows the ionized electrons. A large fraction are expelled by the ponderomotive force, but about ten percent of the electrons remain close to the axis and move forward with the field. The left part shows the electrons that move with $\gamma > 10$. Among those electrons, a few are escaping due to the ponderomotive force and the majority are trapped

trapping and dragging. Figure 8.15 shows only the electrons with v > 0.9 c for different times. The structure is clear, there is a group of trapped electrons that are bouncing back and forth inside the OAM axial node (transverse motion) at the same time that this motion induces a longitudinal drift in accordance to Eq. (8.5). In this back and forth oscillation some electrons escape and generate a flat pattern clearly visible in Fig. 8.15. The same pattern of a central trapped part and escaping cloud is seen in Fig. 8.16 (for the same pulse parameters). At the right part of this figure we depicted only the electrons moving with $\gamma > 10$, while at the left part we plotted all ionized electrons. The structure at the left shows a circle of electrons ionized at the outer part of the field that due to the low intensity are not pushed forward while the inner electrons are expelled generating some sort of bag or fish trap (with the helical structure induced by the OAM helical phase). Electrons at the center are trapped and move forward quickly giving the high density tip. For this case about 9.5 percent of the ionized electrons are trapped and accelerated to $\gamma > 10$ and about one percent of them have a relativistic factor $\gamma > 100$. The attractive (concave) region of the OAM beam corresponds to a radius of about 0.7 w_0.

8.7 Numerical Results for Delayed Mode Superpositions

Now we can analyze combinations of the ($\times$00) mode with only one of the other four modes conveniently shifted in time. The offset is of the order of the pulse duration, or less (otherwise the overlap won't be relevant), and the gaussian pulse is the last to arrive. In this case ponderomotive force shows other interesting features. Some of them can be more or less foreseen from the above considerations and we will skip them, but other features are also surprising and interesting.

Electron steering

Among the surprising possibilities of the different combinations of such modes with different offsets, one of the most relevant is the possibility of electron steering. Combining conveniently the pulses we may get potentials able to deflect electrons. One example of these kind of pulses is the combination ($\times$00) + ($\times$10). Being that the two are polarized in the same direction there will be interference, and the fields add up on one side and show destructive interference on the other side of the 10 nodal plane. Thus, the potential will deviate the electrons to the region of destructive interference because there the intensity is lower. To be sure that the deviation is due to this effect we may compute three different combinations ($\times$00) + ($\times$10), ($\times$00) + i($\times$10), and ($\times$00)-($\times$10).

Results are shown in Fig. 8.17, in all cases the offset is 8 μm(10 cycles) with the (10) mode advanced with respect to the (00). The superpositions ($\times$00) + ($\times$ 10) and the ($\times$00)-($\times$10) are equivalent, deflecting electrons towards the destructive interference side. However the ($\times$00) + i($\times$10) has a symmetrical structure and does not steer electrons. Such combinations are feasible experimentally and moreover a super high intensity is not needed., Thus, ponderomotive steering has a lot of potential

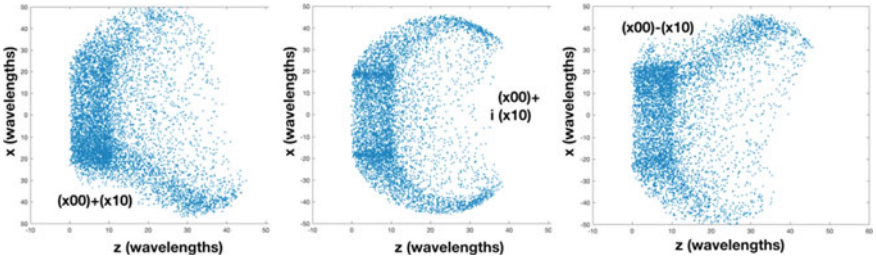

Fig. 8.17 The destructive interference in one side and constructive on the other, generates a ponderomotive force along x that deflects electrons to the region of lower total field. Simulation corresponds to $E_0 = 17$ a.u. (peak at 10^{19} W/cm^2 for the ($\times$00) mode and at 1.8 10^{18} W/cm^2 for the ($\times$10) mode) and 8 microns offset, and for a time 65 cycles after t_0. Electrons born at the edges of the pulse have a very small drift and they constitute the cloud seen between z = 0 and z = 10 wavelengths

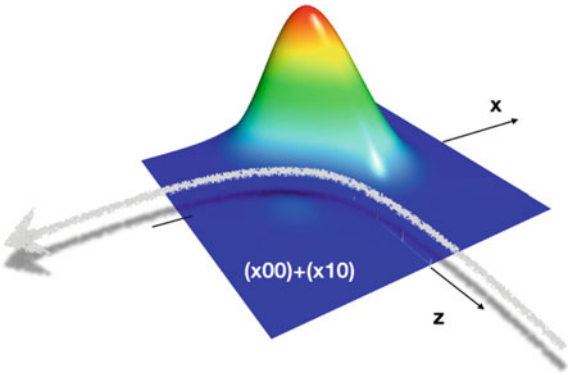

Fig. 8.18 Representation of a cut along the y = 0 plane of the ($\times$00) + ($\times$10) pulse, for 10 cycles offset. Grey arrow indicates the path of the deflected electrons

for coherent control of ionized electrons. Such pulses can push electrons out of one side of the target in a real experiment (Fig. 8.18).

The number of combinations is very large and with five modes and different configurations it is possible to reproduce a huge number of experimental configurations. For example, it is possible to model the horseshoe (or concave) beams, as proposed by Brijesh et al. [30]. They introduced for the first time to our knowledge the concept of concave beams for trapping not only in the transverse directions but also in the longitudinal direction the electrons. Their discussion is very interesting at the onset of the relativistic regime, however, when the dynamics is highly relativistic, electron's drift dominates.

Concave pulses with a gaussian and an OAM mode

To end this investigation of ponderomotive dynamics, let's consider Brijesh horseshoe pulses. The can be modelled here as a combination of the (x00) gaussian pulse and a y-polarized OAM pulse with a few cycles offset. According to our notation those pulses will be ($\times$00) + 2(y10) + 2i(y01), with a 5 cycles offset (always the

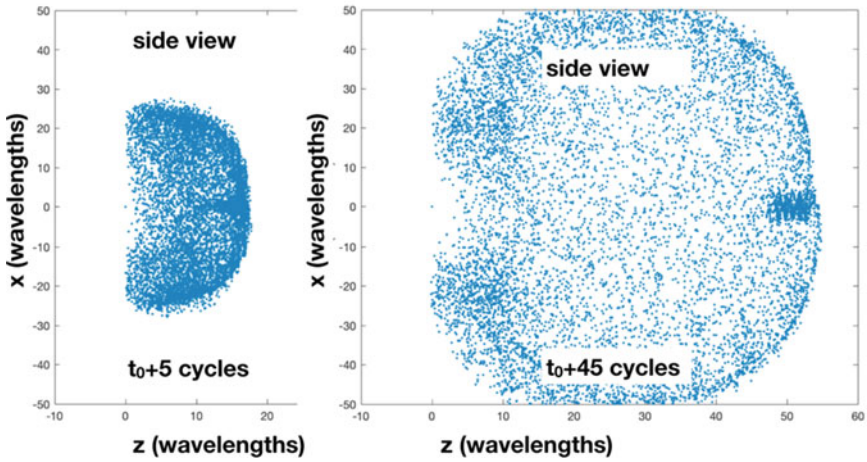

Fig. 8.19 Side views of the electron cloud, during the interaction with the pulse (rigth) and just at the beginning (left). This figure corresponds to a highly relativistic case with $E_0 = 170$ a.u., and a pulse structure $(\times 00) + 2(y10) + 2i(y01)$, with a 5 cycles offset. This corresponds to 10^{21} W/cm^2, peak intensity, for the (00) mode, and 7.4 10^{20} W/cm^2 for each one of the other two

donut in front of the gaussian). Results for that case are shown in Fig. 8.19 for a strongly relativistic case. One can see that the drift of the electron cloud is similar to that observed in Figs. 8.13 and 8.14 for the pure donut or OAM modes themselves and the observed trapped high energy electrons are mainly due to the OAM forward drift itself. The figure corresponds to $E_0 = 170$ a.u. for the gaussian beam (10^{21} W/cm^2). Combining such a peak power gaussian pulse with a similar donut pulse both having smooth profiles is probably on the limit of today's multi PW lasers.

8.8 Conclusions

The ponderomotive potential is ubiquitous in any strong-field experiment where a laser pulse is focused to a small spot. In most cases this is a force that drives electrons out of the focal volume, i.e. it is a force that repels electrons out of the high intensity spot. However, there are modes with a nodal structure that allow trapping and steering of the ionized electrons. While this can readily be understood in the classical or mildly relativistic regime, as intensities enter the 10^{21} W/cm^2 region drifts play a fundamental role in enhancing the trapping and dragging of electrons. With the new multi petawatt lasers and the use of higher order modes, there are a large set of pulse configurations that can be explored and exploited for various applications in electron trapping and steering.

All the present notes are based on the simulation of the Lorentz force dynamics for independent relativistically driven electrons, and without considering nonlinear

effects on the laser propagation. Therefore, the validity of the present results is just for very dilute gases. Study at higher densities would require more complex simulation tools as PIC codes.

Such tools to control the electron dynamics while electrons are still driven by the intense pulse may result in interesting applications such as injection to other accelerators or boosters. Also new coherent radiation schemes seem possible because electrons are self-organized in patterns by the relativistic dynamics. At the present low densities, the number of emitted photons will be small.

Acknowledgements We acknowledge support from the Spanish Ministerio de Ciencia, Innovación y Universidades and the European Regional Development Fund (Grants No. FIS2016-81056-R, and EQC2018-005230-P), from H2020-EU Laserlab Europe V (Grant No. 871124), from Junta de Castilla y León (Grant No. CLP087U16), and from the Natural Sciences and Engineering Research Council of Canada (Grant No. RGPIN-2019-05013).

References

1. T.W.B. Kibble, Mutual refraction of electrons and photons. Phys. Rev. **150**, 1060 (1966)
2. D. Strickland, G. Mourou, Compression of amplified chirped optical pulses. Optics Communications **55**, 447–449 (1985)
3. C. Danson et al., Petawatt and exawatt class lasers worldwide. High Power Laser Science and Engineering **7**, E54 (2019)
4. E. Esarey, C.B. Schroeder, W.P. Leemans, Physics of laser-driven plasma-based electron accelerators. Rev. Mod. Phys. **81**, 1229 (2009)
5. P. M. Woodward, A method for calculating the field over a plane aperture required to produce a given polar diagram, J. Inst. Electr. Eng., 93 Part IIIA (1947) 1554
6. F. Amiranoff et al., Observation of laser wakefield acceleration of electrons. Phys. Rev. Lett. **81**, 995 (1998)
7. V. Malka, Laser plasma accelerators, Phys. Plasmas, 19 (2012) 055501.
8. S. Kneip et al., Bright spatially coherent synchrotron X-rays from a table-top source. Nat. Phys. **6**, 980 (2010)
9. E. Esarey, P. Sprangle, J. Krall, Acceleration of electrons invacuum. Phys. Rev. E **52**, 5443 (1995)
10. J. San Roman, L. Roso and H. Reiss, Evolution of a relativisitic wavepacket describing a free electron in a very intense laser field, J Physics B: Atom Molec Opt Phys, 33 (2000) 1869
11. J. San Roman, L. Roso and L. Plaja, A complete description of the spin force, J Physics B: Atom Molec Opt Phys, 36 (2003) 1
12. I. C. E. Turcu, et al., Quantum electrodynamics experiments with colliding petawatt laser pulses, High Power Laser Science and Engineering 7 (2019).
13. E.S. Sarachik, G.T. Schappert, Classical theory of the scattering of intense laser radiation by free electrons. Physical Review D **1**, 2738 (1970)
14. C.I. Moore, J.P. Knauer, D.D. Meyerhoffer, Observation of the transition from Thomson to Compton scattering in multiphoton interactions with low-energy electrons. Phys Rev Letters **74**, 2439 (1995)
15. C. H. He, et al., Towards an in situ, full-power gauge of the focal-volume intensity of petawatt-class lasers, Optics Express 27 (2019)
16. I. Pastor, et al., Nonlinear relativistic electron Thomson Scattering for laser radiation with orbital angular momentum, Journal of Physics Communications, 4 (2020) 065010.

17. J. Pang, et al., Subluminous phase velocity of a focused laser beam and vacuum laser acceleration, Physical Review E, 66 (2002) 066501
18. J.D. Lawson, Lasers and Accelerators, , IEEE Trans. Nucl. Sci. NS- **26**, 4217 (1979)
19. P. M. Woodward, A method of calculating the field over a plane aperture required to produce a given polar diagram, J. Inst. Electr. Eng., 93 Part IIIA (1947) 1554
20. P. Gibbon, Short pulse laser interactions with matter: an introduction. World Scientific, 2005.
21. N. Cao et al., Accurate description of gaussian beams and electron dynamics. Optics Communications **204**, 7 (2002)
22. L.W. Davies, Vector electromagnetic modes of an optical resonator. Phys. Rev. A **19**, 1177 (1979)
23. W. Kochner, Solid-State Laser Engineering, Springer, 2006
24. N.J. Phillips, J.J. Sanderson, Trapping of electrons in a spatially inhomogeneous laser beam. Physics Letters **21**, 533 (1966)
25. C.I. Moore, Confinement of electrons to the centre of a laser focus via the ponderomotive potential. J. Mod. Opt. **39**, 2171 (1992)
26. S. Miyazaki et al., Generation of a microelectron beam by an intense short pulse laser in the TEM(1,0)+TEM(01) mode in vacuum. J Phys D: Applied Physics **38**, 1665 (2005)
27. M. Padgett et al., An experiment to observe the intensity and phase structure of Laguerre-Gaussian laser modes. Am. J. Phys. **64**, 1 (1996)
28. A. Longman, R. Fedosejevs, Mode conversion efficiency to Laguerre-Gaussian AOM modes using spiral phase optics. Opt. Express **25**, 17382 (2017)
29. A. Longman et al., Off-axis spiral mirrors for generating high-intensity optical vortices. Opt. Lett. **45**, 2187 (2020)
30. P. Brijesh et al., Demonstration of a horseshoe-shaped longitudinal focal profile. J Optical Society of America B **24**, 1030 (2007)